Article:
Davies, CJ and Constable, CG (2018) Searching for Geomagnetic Spikes in Numerical Dynamo Simulations. Earth and Planetary Science Letters, 504. pp. 72-83. ISSN: 0012-821X

https://doi.org/10.1016/j.epsl.2018.09.037

Searching for Geomagnetic Spikes in Numerical Dynamo Simulations

Christopher J. Davies[a,b], Catherine G. Constable[b]

[a] *School of Earth and Environment, University of Leeds, Leeds LS2 9JT, UK (tel: +44 (0) 113 34 31140; email: c.davies@leeds.ac.uk*

[b] *Institute of Geophysics and Planetary Physics, Scripps Institution of Oceanography, University of California at San Diego, La Jolla, CA, 92092-0225, USA*

Abstract

We use numerical dynamo simulations to investigate rapid changes in geomagnetic field intensity. The work is motivated by paleomagnetic observations of 'geomagnetic spikes', events where the field intensity rose and then fell by a factor of 2-3 over decadal timescales and a confined spatial region. No comparable events have been found in the historical record and so geomagnetic spikes may contain new and important information regarding the operation of the geodynamo. However, they are also controversial because uncertainties and resolution limitations in the available data hinder efforts to define their spatio-temporal characteristics. This has led to debate over whether such extreme events can originate in Earth's liquid core. Geodynamo simulations produce high spatio-temporal resolution intensity information, but must be interpreted with care since they cannot yet run at the conditions of Earth's liquid core. We employ reversing and non-reversing geodynamo simulations run at different physical conditions and consider various methods of scaling the results to allow comparison with Earth. In each simulation we search for 'extremal events', defined as the maximum intensity difference between consecutive time points, at each location on a 2° latitude-longitude grid at Earth's surface, thereby making no assumptions

regarding the spatio-temporal character of the event. Extremal events display spike-shaped time-series in some simulations, though they can often be asymmetric about the peak intensity. Maximum rates of change reach 0.75 $\mu T yr^{-1}$ in several simulations, the lower end of estimates for spikes, suggesting that such events can originate from the core. The fastest changes generally occur at latitudes $> 50°|$, which could be used to guide future data acquisitions. Extremal events in the simulations arise from rapid intensification of flux patches as they migrate across the core surface, rather than emergence of patches from within the core. The prospect of observing more spikes in the paleomagnetic record appears contingent on finding samples at the right location and time to sample this particular phase of flux patch evolution.

Keywords: Geodynamo simulations, Secular variation, Geomagnetic spikes, Earth's core

1. Introduction

Paleomagnetic data provide some of the few available constraints on long term variations in geomagnetic field strength, but do not yet precisely determine how rapidly the field can change or what upper limits exist on absolute field strength. The term 'geomagnetic spike' was originally used to describe extreme changes in the intensity F of Earth's magnetic field recorded in Jordanian and Israeli copper slag piles around 1000 BCE (Ben-Yosef et al., 2009). The original data showed spikes at 980 BCE and 890 BCE with the Virtual Axial Dipole Moment (VADM) rising from $\approx$140 ZAm^2 to $220 - 260$ ZAm^2 followed by a similarly sharp decline, all in less than 30 yrs (Shaar et al., 2011). These values are much larger than the mean dipole strength of the modern and Holocene field, 80 ZAm^2 (Thébault et al., 2015) and 95 ZAm^2 (Constable et al., 2016) respectively. The apparent rate of intensity change, $\partial F/\partial t$, is also remarkably rapid. Livermore et al. (2014) fit smooth

functions through the Shaar et al. (2011) data and find that $\partial F/\partial t = 4 - 5\ \mu T yr^{-1}$, significantly larger than global values of about $0.12\ \mu T yr^{-1}$ (Thébault et al., 2015) for the modern field and the averages over Holocene field models (Korte and Constable, 2018). Subsequent studies have added more data in the Levant region and applied more robust selection criteria to the original data, finding lower peak VADM's of $\approx$190 ZAm^2 (Shaar et al., 2016) and slower rates of change of $\partial F/\partial t = 0.75 - 1.5\ \mu T yr^{-1}$ (Ben-Yosef et al., 2017). Nevertheless, these values are some of the highest ever obtained and mark out the Levantine geomagnetic spike as one of the most extreme variations of Earth's magnetic field ever recorded.

The Levantine geomagnetic spike was probably not a global phenomenon. High VADM's similar to those acquired in Jordan and Israel were found in Turkey (Ertepinar et al., 2012) and Georgia (Shaar et al., 2013) around 1000 BCE and in China (Cai et al., 2017) around 1300 BCE. Conversely, low VADM's around 1000 BCE similar to the mean Holocene value were obtained in Cyprus (Shaar et al., 2015), Bulgaria (Kovacheva et al., 2014), Syria (Gallet et al., 2015) and across Europe (Kapper et al., 2015). Extreme values of F and $\partial F/\partial t$ have also been reported from sediments in Halls Cave, Texas, around the same time (Bourne et al., 2016), though these likely reflect a different underlying geomagnetic feature (Davies and Constable, 2017). Such localised features are not seen in global time-dependent Holocene fields models such as pfm9k, CALS10k.2 or HFM.OL1.A1 (Nilsson et al., 2014; Pavòn-Carrasco et al., 2014; Constable et al., 2016), which are necessarily smoothed in both space and time owing to the uneven and limited spatio-temporal distribution of the underlying dataset.

In attempting to map the potential spatial structure of the spike Davies and Constable (2017) used a Fisher-Von Mises probability distribution and fit the amplitude, width and location of this function to the Geomagia.v3 dataset (Brown et al.,

2015) together with newer spike data. By minimising the L^1 misfit between data and the Fisherian representation, weighted by the data uncertainties, they found a best-fitting spike characterised by closed intensity contours and centred under Saudi Arabia. They also showed that, in order for the spike to originate in Earth's liquid core, a factor of 2 rise and fall in F at Earth's surface can only occur over a region that spans at least 60° longitude. The corresponding feature at the core-mantle boundary (CMB) must be remarkably localised, spanning only a few degrees longitude. This suggests that the Levantine spike was highly localised in both space and time.

However, despite some progress geomagnetic spikes remain enigmatic and controversial. The original published values of F and $\partial F/\partial t$ for Israel (Shaar et al., 2011) were subsequently lowered (Shaar et al., 2016) and the application of more stringent selection criteria led to the rejection of the 890 BCE spike and the proposal of a new spike at 800 BCE. Even when adopting these new data the synthetic spike of Davies and Constable (2017) cannot simultaneously match the high VADM's in Jordan and Israel and the low VADM's in Syria and Cyprus. This may be due to age uncertainties, such that low intensity data sampled the field before the spike, though it could be interpreted as evidence that the spike geometry is incompatible with an origin in Earth's core. Livermore et al. (2014) used an optimisation procedure to argue that the maximum rates of change that could arise from core flow are $0.6 - 1.2\ \mu T yr^{-1}$, too small to explain the rates of $4 - 5\ \mu T yr^{-1}$ they inferred for the Levantine spike but more consistent with the newer spike data. Their method also requires knowledge of the RMS core surface velocity, which is unknown at the time of the spike and therefore allows some flexibility in the result. Nevertheless, the flow structure predicted by Livermore et al. (2014) is highly localised and very different from anything inferred from the modern field or from geodynamo simula-

tions, raising the question of how such a profound change occurred over a timescale that is short in the context of core dynamics. These issues led Fournier et al. (2015) to seek corroborative evidence for the existence of spikes using cosmogenic nuclides, although they returned equivocal results.

Korte and Constable (2018) recently investigated whether spike-like features are associated with motion and/or growth and decay of intense equatorial flux patches like those seen in the modern field (Jackson, 2003). The data are compatible with growth of such features in a confined region, and possible later migration to the north and west (Davies and Constable, 2017). The analysis of Korte and Constable (2018) suggests that spike data support higher intensity and greater variability of the dipole moment than in most Holocene field models, but do not appear to require excessively strong rates of change.

Much of the uncertainty and controversy surrounding geomagnetic spikes stems from the limited spatio-temporal sampling and age controls provided by the available data. The spike morphology and associated rates of change are still rather poorly constrained. Further observations (or confirmed absences) of spike-like features are crucial, but it is not clear where or when to look. Davies and Constable (2017) noted that the Levantine spike occurs at a time when the dipole moment begins to rise from a local minimum, but it is not clear if this is a general causative relation that could be used to indirectly detect spikes. The signature of spikes probably depends on the physical mechanisms that cause them, which are currently unknown. These issues are significant since much insight into the dynamics of Earth's core derives from observations spanning the last few centuries. If spikes do originate in the outer core, they potentially contain important information regarding the operation of the geodynamo that is not contained in the historical record.

We seek independent corroborative evidence for extreme variations of the mag-

netic field using numerical geodynamo simulations. These simulations routinely display fields that are morphologically similar to the historical (Christensen et al., 2010; Mound et al., 2015) and Holocene (Davies and Constable, 2014) field and also produce other geomagnetic phenomena such as polarity reversals. The main advantage of using dynamo simulations is that a dense spatial and temporal sampling can be achieved in runs that span many magnetic diffusion times, equivalent to hundreds of thousands of years. The main disadvantage of the simulations is that they cannot yet run with values for the material properties that characterise Earth's liquid outer core (Davies et al., 2015) and so the results must be interpreted with care. We employ a suite of simulations that have been run with different parameter values so that any systematic trends can be assessed.

We use geodynamo simulations to investigate the following questions pertaining to geomagnetic spikes: 1) Do simulations produce spike-like features, i.e. rapid increases in F followed by a decrease of similar speed and magnitude? If so, do these events have similar rates of intensity change and morphology to those observed in the Levant? 2) Are there preferred locations for extreme intensity changes? Is there any special significance attached to the Levantine region or to the mid-to-low latitudes? 3) Are spike-like features associated with other magnetic variations such as a rise in dipole moment? These issues are a necessary precursor to understanding the physical mechanism responsible for spikes. In section 2 we present the numerical simulations used in this study and a simple algorithm for identifying extreme intensity variations in these models that makes no assumptions regarding the spatio-temporal form of the spike signal. Results are presented in section 3 and a discussion of how to apply these results to Earth is given in section 4. Conclusions are described in section 5. The main result of our study is summarised in Figure 4.

2. Models

We use numerical simulations describing dynamo action of an electrically conducting fluid confined within a rotating spherical shell. The numerical model (Willis et al., 2007) solves the standard Boussinesq equations and has been benchmarked against other codes (Matsui et al., 2016). The simulations used in this study are summarised in Table 1 and are taken from our previous work (Davies et al., 2008; Davies and Gubbins, 2011; Davies and Constable, 2014). They are characterised by the Ekman number E, the magnetic Prandtl number Pm, the Rayleigh number Ra, and the Prandtl number $Pr = 1$, where

$$E = \frac{\nu}{2\Omega d^2}; \quad Pm = \frac{\nu}{\eta}; \quad Ra = \frac{\alpha g(\mathrm{d}T'/\mathrm{d}r)d^4}{\kappa\nu}. \tag{1}$$

Here d is the shell thickness, ν is the kinematic viscosity, Ω is the rotation frequency, η is the magnetic diffusivity, α is the thermal expansivity, g is the gravitational acceleration at the outer boundary of the domain, κ is the thermal diffusivity and $\mathrm{d}T'/\mathrm{d}r$ is the gradient of the perturbation temperature. The ratio of inner core to outer core radii $\xi = 0.35$ in all models. We will refer to these radii as the inner boundary and outer boundary respectively, to distinguish from the inner core boundary and CMB of Earth. All simulations use no-slip velocity boundary conditions and an electrically insulating mantle, while the inner core can be either insulating or conducting. The thermal boundary condition is fixed heat flux on the outer boundary and either fixed flux or fixed temperature on the inner boundary. The outer boundary heat flux can be heterogeneous with a pattern corresponding to the seismic tomographic model of Masters et al. (2000) and an amplitude $q^\star$ defined as the ratio of the peak-to-peak boundary heat flow variations to the average heat flow.

The dynamo simulations used in this study (Table 1) have been selected based

on three considerations. First, the simulations should capture the range of magnetic field variability seen in previous studies (Kutzner and Christensen, 2002; Driscoll and Olson, 2009) ranging from stable dipole-dominated fields to fields that undergo excursions and polarity reversals. Second, the simulations need to be run for as long as possible in order to best capture the range of possible variability at the chosen parameters. Satisfying these two requirements given the vast computational resources required to run long geodynamo simulations (Matsui et al., 2016) necessitates focus on solutions with modest $E \geq 10^{-4}$ and $Pm \geq 1$. Finally, we require that the simulations reproduce aspects of the spatio-temporal behaviour exhibited by the geomagnetic field. To do this we follow the procedure of Davies and Constable (2014), which builds on the work of Christensen et al. (2010) by defining criteria based on the morphology of the historical and Holocene geomagnetic field and on the shape of the temporal power spectrum. Simulations with $E = 1.2 \times 10^{-4}$ (Table 1) show good agreement using all criteria, meaning that they produce field morphologies and power spectra that are similar to the recent geomagnetic field, though they do not exhibit polarity reversals. Simulations with $E = 5 \times 10^{-4}$ show weaker morphological resemblance to the recent geomagnetic field (Davies and Constable, 2014), but produce polarity reversals and excursions.

The simulations in Table 1 employ different combinations of dimensionless parameters and boundary conditions because they were originally designed to study different phenomena. The simulations with $E = 5 \times 10^{-4}$ employ a value of Ra far above the critical Rayleigh number Ra_c for the onset of non-magnetic convection and are therefore strongly driven. They were originally used to investigate long-term variability of gross magnetic field properties (Davies and Constable, 2014). Simulations with $E = 1.2 \times 10^{-4}$ and low $Ra \sim Ra_c$ were tuned to display 'locking' of the magnetic field features to the spatial pattern of boundary heat flow (Gubbins et al.,

2007; Davies et al., 2008). Simulations with $E = 1.2 \times 10^{-4}$ and $Ra \sim 10 - 30Ra_c$ were used to explore the dynamical regime transitions that occur near the region of locked solutions. Following previous work (Christensen et al., 2010; Olson et al., 2012; Davies and Constable, 2014) we discuss simulations in terms of their magnetic Reynolds number, $Rm^m = U^m d/\eta^m$, where U^m is the time-average RMS fluid velocity of the simulations. Our simulations have $Rm^m = 100 - 700$, compared to the value $Rm^E \sim 10^3$ estimated for Earth's core (Olson et al., 2012; Davies et al., 2015). The values of Rm given in Table 1 serve as a useful and unique means of identifying our individual numerical simulations.

Field intensity F at radius $r = a$ corresponding to Earth's surface (hereafter referred to simply as "the surface") is generated from the poloidal field $B_P(r_c)$ at the outer boundary of the dynamo simulations, radius $r = r_c$. $B_P(r_c)$ is saved every 200-500 timesteps (in order to minimise overall storage costs) as a set of complex Schmidt quasi-normalised spherical harmonic coefficients c_l^m, where l and m denote harmonic degree and order respectively. The c_l^m may be converted into Gauss coefficients g_l^m and h_l^m at $r = a$ using the standard definition of the potential outside the core and the definition of the poloidal potential in the dynamo code (Willis et al., 2007):

$$\begin{aligned} g_l^0 &= -\frac{\Re(c_l^0)l}{r_c}\left(\frac{r_c}{a}\right)^{(l+2)}, h_l^0 = 0 \text{ for } m = 0 \\ g_l^m &= -2\frac{\Re(c_l^m)l}{r_c}\left(\frac{r_c}{a}\right)^{(l+2)}, h_l^m = 2\frac{\Im(c_l^m)l}{r_c}\left(\frac{r_c}{a}\right)^{(l+2)} \text{ for } m \neq 0 \end{aligned}$$

The Gauss coefficients are then used to compute the magnetic elements $X(a, \theta, \phi, t)$, $Y(a, \theta, \phi, t)$, $Z(a, \theta, \phi, t)$ and $F(a, \theta, \phi, t)$ on a 2° by 2° latitude-longitude (θ, ϕ) geographic grid.

The primary observational feature of spikes is the high $\partial F/\partial t$ and so we focus

on this as the diagnostic of extreme intensity variations. Each dynamo simulation consists of $O(10^4 - 10^6)$ timesteps and at each step the chosen grid produces values of F at over 15,000 locations. We therefore require an algorithm that can extract the most extreme intensity variations from these large datasets. Our strategy is to compute at each θ, ϕ point the maximum rate of change in F between two saved states of the magnetic field, which are separated by a time Δt:

$$\left.\frac{\partial F}{\partial t}\right|_{\max} = \left.\frac{F(t) - F(t - \Delta t)}{\Delta t}\right|_{\max}. \tag{2}$$

This procedure deliberately makes no assumption regarding the morphology of the 'spike' event. It only identifies the most rapid increase in intensity, and can potentially ignore an event with more gradual temporal evolution that might lead to a stronger peak field, followed by an intensity decrease of similar speed and magnitude, as such events will not be the fastest events recorded in the simulation. We are only interested in rapid changes and not in spike-shaped temporal events that are much too slow to be representative of the observations. In section 4 we assess our method in the context of the results.

Since the dynamo simulations work with dimensionless variables both F (units of μT) and t (units of yrs) must be computed from their dimensionless counterparts $F^\star$ and $t^\star$. For F we attempt two plausible scalings. Scaling (1) uses Elsasser units, $F = (2\Omega\rho\mu_0\eta)^{1/2} F^\star$, which is the scaling used in our dynamo code (Willis et al., 2007) and in many previous studies (e.g. Olson and Christensen, 2002; Davies et al., 2008; Heimpel and Evans, 2013). We use $\Omega = 7.272 \times 10^{-5}$ s^{-1}, $\rho = 10^4$ kg m^{-3} for the density near the CMB (Dziewonski and Anderson, 1981), $\mu_0 = 4\pi \times 10^{-7}$ N A^{-2} for the permeability of free space and $\eta = 1$ m^2 s^{-1} (Davies et al., 2015). With this scaling $F = 1351.9 F^\star\ \mu T$ for all runs. The problem with scaling (1) is that F

varies significantly between different dynamo simulations. In scaling (2) the time-average intensity at the south pole is set to 70 μT, which corresponds to the average VADM value of 95 ZAm^2 from the CALS10k.2 field model (Constable et al., 2016). The problem with this scaling is that it is somewhat arbitrary, though it has also been used in several previous studies (e.g. Jones, 2014; Driscoll, 2016). By using two different scalings for F we are able to quantify their effect on $\partial F/\partial t$.

In the dynamo simulations (denoted by superscript m), time is scaled by the magnetic diffusion timescale, i.e.

$$t = \frac{d^2}{\eta} t^\star = \tau_d^m t^\star = Rm^m \tau_a^m t^\star, \tag{3}$$

where $\tau_m^a = d/U^m$ is the simulation advection time and $Rm^m = \tau_d^m/\tau_a^m$ (Olson et al., 2012; Davies and Constable, 2014). The magnetic Reynolds number of Earth $Rm^E = \tau_d^E/\tau_a^E$. Our interest in short timescale phenomena suggests rescaling to dimensional time using the advection timescale (Olson et al., 2012), $\tau_a^m = \tau_a^E$, and hence $t = (Rm^m \tau_d^E/Rm^E)t^\star$. We use $d = 2264$ km, and $Rm^E = 900$, for which $\tau_d^E = 165.5$ kyrs and $t = 54t^\star$ kyrs. With this scaling Δt (equation 2) is typically less than a decade, though this varies between simulations and within an individual simulation since our numerical code adaptively sets the timestep size. Note that using the diffusion timescale would predict slower variations by a factor of Rm^E/Rm^m.

It what follows it will sometimes prove useful to isolate intensity variations at low latitudes. We set a cutoff latitude, θ_c, such that only data at latitudes lower than θ_c are retained. Clearly $\theta_c = 90^\circ$ means that all data are retained. The value $\theta_c = 35^\circ$ on $r = a$ is suggested by the Levantine spike.

3. Results

We first provide a detailed description of results with intensity scaling (2) and no latitudinal cutoff before demonstrating how changing the intensity scaling and cutoff changes the main results. Simulations are summarised in Table 1. Figure 1 summarises the intensity variability at the surface for $Rm = 135$ and 252. All simulations with a homogeneous outer boundary produce almost axisymmetric time-averaged fields, while low Rm dynamos with outer boundary heat flow heterogeneity can produce significant longitudinal variations in average intensity with a dominant spherical harmonic degree 2 contribution (Gubbins et al., 2007; Davies et al., 2008). Increasing Rm increases the spatio-temporal variability in F and simulations that reverse can produce very low intensities at all locations. Maximum variability occurs at high latitudes in all simulations and reflects the movement of intense flux patches (e.g. Olson and Christensen, 2002; Kutzner and Christensen, 2002; Davies et al., 2008).

To isolate the most rapid intensity variations Figure 2 shows maps of $(\partial F/\partial t)_{\max}$ for eight of the nine simulations. The values of $(\partial F/\partial t)_{\max}$ plotted at each point may occur at different times, which explains the jagged features in these plots. At low latitudes $(\partial F/\partial t)_{\max}$ can vary in longitude by a factor of 3-8, with slightly larger variations associated with strong thermal outer boundary variations or reversals; across the suite of simulations it varies by a factor of 3-10 with the largest values generally at high latitudes. The significant longitudinal variations in $(\partial F/\partial t)_{\max}$ in all cases arise because the algorithm deliberately samples extreme values of the local intensity distribution. We would expect these variations to decrease upon running the simulations for longer, though it is interesting to note that they persist for well over 10 magnetic diffusion times in some cases.

Time-series of F and $\partial F/\partial t$ at the locations of maximum intensity change, highlighted by white dots in Figure 2 and denoted $\theta_{\max}$ in Table 1, are shown in Figure 3. We refer to these events as 'extremal events', since they are the fastest changes in F produced by a given simulation. In the runs with $Rm = 135$ and 450 a spike-like feature is identified with a sharp intensity rise followed by a rapid decline of comparable magnitude and speed, similar to that seen in the Levant. A spike-like extremal event is also identified in the simulation with $Rm = 108$, though the intensity before and after the event are markedly different, while the extremal event in the $Rm = 684$ simulation has a sharp rise and fall in F with a short flat segment in between. The extremal event in the simulation with $Rm = 225$ occurs during a sharp increase in F, but the following decrease is much slower. Clearly the simulations produce spike-like temporal variations, though there is significant variability in the details of the signal.

In the other simulations shown in Figure 3 the extremal event identified by our method does not display a spike-shaped temporal evolution. For simulations with $Rm = 252$ and 386 this event occurs directly after a local minimum in F, while in simulations with $Rm = 351$ and 540 the event occurs during a slow increase in F. This does not mean that no spike-like events occurred in the simulation; however, if they did the rate of change was slower than for the extremal event identified. Put another way, the fastest changes are not spike-like in these dynamos. Since the rates of change identified in these simulations are already at the low end of estimates attributed to the Levantine spike, any spike-like features are unlikely to be representative of the Levantine spike.

Figure 4 summarises the main results for both F scalings and two values of the latitudinal cutoff: $\theta_c = 90°$ and $\theta_c = 35°$. Recall that θ_c is defined such that all data are removed for latitudes above $|\theta_c|$. The scaling that yields the highest $(\partial F/\partial t)_{\max}$ varies between simulations because the conversion between dimensionless

and dimensional values using scaling (2) is simulation-dependent. However, both scalings produce essentially identical spatial structure in $(\partial F/\partial t)_{\max}$ maps (Figure 2). The value of θ_c does not greatly influence the results because the extremal events arising at lower latitudes are caused by temporary excursions of the high-latitude flux patches. Values of $(\partial F/\partial t)_{\max}$ exceed the present field value in all simulations, for both F scalings and both θ_c values. Some simulations produce values of $(\partial F/\partial t)_{\max}$ at or above the rates inferred by Ben-Yosef et al. (2017), but all are over a factor of 3 lower than the rates inferred by Livermore et al. (2014) based on the Levantine spike data of Shaar et al. (2011). This result has no clear dependence on Rm for our chosen simulations. There is a factor or 3-10 variation of $(\partial F/\partial t)_{\max}$ with position. The location of maximum intensity change, $\theta_{\max}$, is pole-ward of $|50°|$ in all except one simulation and always outside the tangent cylinder, which again reflects the presence of high-latitude flux patches.

To investigate the physical characteristics of extremal events Figures 5 and 6 show snapshots of the radial magnetic field B_r at the surface and outer boundary for simulations with $Rm = 108$ and $Rm = 450$ respectively. In the $Rm = 108$ solution the extremal event occurs in the southern hemisphere and is preceded by a patch of intense normal polarity flux emerging at the outer boundary north-east of the location of maximum $(\partial F/\partial t)_{\max}$. The patch intensifies as it migrates south-west and the extremal event occurs just before the patch passes beneath the observation point. There is little expression of the outer boundary flux patch at the surface and indeed the surface feature bears little resemblance to the spike morphology inferred by Davies and Constable (2017). Similar behaviour is seen in the simulation with $Rm = 450$ for an extremal event in the northern hemisphere. Interestingly we do not find any extremal events that correspond to emergence of flux from the deeper core directly under the observation point.

Finally, we consider in Figure 7 the relationship between extremal events and changes in dipole moment for simulations with $Rm = 108$, 252, and 450. The extremal events in the simulations with $Rm = 108$ and $Rm = 450$, which appear as spike-like intensity variations (Figure 3), occur at times when the dipole moment is above average, but not close to its maximum value. In the $Rm = 252$ simulation the extremal event does occur when the dipole moment is high. In all cases extremal events occur when the dipole moment is growing. Poleward migration of normal polarity flux as seen in Figures 5 and 6 will increase the dipole moment; however, the net effect will depend on both poleward and equatorward migration of reversed and normal polarity flux (Finlay et al., 2016), which we have not investigated in detail. It is thus not clear at present whether dipole moment growth is a general feature that accompanies extremal events.

4. Discussion

Before seeking to apply our results to the Earth it is important to assess the limitations of our approach. The inherent limitations with the present generation of numerical geodynamo simulations mean that the possibility of generating faster intensity variations in simulations with more Earth-like parameters cannot be ruled out. Recent dynamo simulations that reach Ekman numbers $E \sim 10^{-7}$ and Rayleigh numbers Ra many times the critical value find the emergence of fast hydromagnetic waves with decadal and sub-decadal periods (Schaeffer et al., 2017; Aubert, 2018) that are less prominent or absent at less geophysically relevant conditions. The spatially localised and inherently aperiodic nature of extremal events suggests that they reflect bulk fluid motion rather than propagation of hydromagnetic waves. However, the magnetic force also appears to play a greater role in these simulations, which could affect extremal events.

Scaling laws are required to systematically compare general system behaviour as individual parameters are varied. Scaling laws tested on conventional dynamo simulations (Stelzer and Jackson, 2013; King and Buffett, 2013) suggest some dependence of the characteristic flow speed, measured by the Reynolds number Re, on the diffusion coefficients: Re increases with Ra, but decreases with decreasing E. The dominant effect at core conditions ($E \sim 10^{-15}$, $Ra \geq 1000 Ra_c$) is hard to establish because i) scaling laws cannot be tested in this regime; ii) scaling laws predict similar dependencies of Re on Ra and E and; iii) Ra is hard to estimate for the core. Aubert et al. (2017) have used large eddy simulations, which parameterise the smallest scales and thus allow lower E than convection dynamo simulations, to argue that Re follows a diffusionless scaling (Christensen and Aubert, 2006), suggesting that Re should increase as more Earth-like parameters are approached. Since Rm is also large in the core, this might suggest greater variability of the magnetic field at more extreme conditions. However, it is unclear whether these results can be applied to extremal events because Re is a temporally and spatially averaged measure of the flow speed, while extremal events are by definition strongly localised in space and time. Indeed, the simulations in Schaeffer et al. (2017) show significant spatio-temporal variations in the force balance and dynamical regimes, suggesting that simple scaling laws are unlikely to adequately predict the properties of extremal events.

Incorporating additional physical effects into the simulations may influence the locations and amplitudes of extremal events. Aubert (2013) and Mound et al. (2015) found flux spots near the equator in simulations with heat flow heterogeneity on the inner and outer boundaries, with Aubert (2013) also employing a stress-free outer boundary (as opposed to the no-slip velocity condition used here), and gravitational coupling between the inner core and mantle (absent in the present simulations).

Whether or not to include such effects is still a matter of debate. It now seems unlikely that the inner core can support significant lateral heat flow variations with the high thermal conductivity predicted by *ab initio* calculations (Pozzo et al., 2014), although different possible instabilities for driving inner core convection are still being investigated (see Wong et al., 2018; Deguen et al., 2018, for recent discussion). No-slip velocity conditions are the physically relevant choice, but produce Ekman layers in the simulations that are much thicker than in Earth's core, which likely affect the dynamics near the outer boundary; stress-free conditions remove the Ekman layer all together and also alter other aspects of the dynamics such as the zonal flow. In our simulations the amplitude of outer boundary heat flow variations does not significantly affect the location and amplitude of extremal events and so we might expect a similar result to apply to lateral variations at the inner boundary. Gravitational coupling and stress-free boundary conditions may influence extremal events by driving flows near the outer boundary. The actual role of these processes and possible changes in system behaviour at lower E and higher Ra than we consider will required detailed analysis in future studies, which can be investigated using the algorithm developed here.

All simulations used in this work assume that the mantle is an electrical insulator. Lower mantle conductivity is poorly constrained, but it could be significant in localised regions if zones of anomalously low seismic velocity reflect iron enrichment (e.g. Garnero et al., 2016). The expected effect of a conducting layer above the CMB is to smooth and delay magnetic variations originating in the core (Backus, 1983). Smaller lengthscale features are preferentially attenuated, but since the extremal events predicted by our models are already smooth and large-scale at the surface (Figures 5 and 6) we expect that including a conducting lower mantle would have very little effect. The time delay induced by the conducting layer is irrelevant here

because time is arbitrary in the simulations, though it might be relevant for analysing the origin of spikes in Earth.

Despite these issues, our suite of simulations display consistent results: Figure 4 shows no obvious dependence on Rm of either the location or amplitude of $(\partial F/\partial t)_{\max}$, none of the simulations produce surface extremal events that resemble the morphology comprising closed intensity contours suggested by Davies and Constable (2017) for the Levantine spike, and the $(\partial F/\partial t)_{\max}$ values are comparable to the bounds inferred by Livermore et al. (2014) using a completely different approach. The simulations produce a range of extremal events–some look like spikes and some do not–and it may be that one type of event is preferred as Earth-like parameters are approached, though we have no way to test this possibility. Overall we believe the simulations display a range of plausible behaviour and provide a consistent picture of rapid intensity changes.

The choice of scaling used to convert intensity output from the simulations into dimensional units has no influence on the predicted spatial characteristics of extremal events. The scaling does affect the predicted values of $(\partial F/\partial t)_{\max}$, but not by enough to change the conclusions described above. Other scalings are possible, in particular those derived from scaling analysis of the governing equations. However, various scaling laws for the field strength have been proposed (Christensen, 2010) and all rely on poorly known quantities such as the CMB heat flow or electrical conductivity of the core material. In view of these limitations we believe that our use of two different plausible intensity scalings sufficiently demonstrates their effect.

We also assumed an advective scaling for the time axis. Adopting instead a scaling based on the magnetic diffusion time would lower the predicted values of $(\partial F/\partial t)_{\max}$ by a factor of Rm^E/Rm^M, likely moving them below the values of Ben-Yosef et al. (2017) but still within the range suggested by Korte and Constable

(2018). Other aspects of our conclusions are unchanged by this choice. However, previous studies have shown that short timescale behaviour is best represented by the advective timescale (Lhuillier et al., 2011; Olson et al., 2012) and we have followed this here.

Our method for identifying extreme intensity variations finds the fastest change in F between two saved states of the simulation separated by time Δt and therefore does not consider longer temporal correlations. For example, at a single location the method would not identify a spike-shaped temporal feature that consists of three consecutive intensity increases followed by three equal intensity decreases unless one of the increases was the fastest increase at that location. Consequently, even though some simulations in Figure 3 do not show spike-like temporal features this does not rule out the possibility that such a feature exists somewhere in the simulation. However, any such 'composite spike' must evolve more slowly than the rates shown in Figure 4 and so this possibility does not affect our conclusions regarding rates of change; indeed, the slower evolution of these features raises the question of whether they bear any relation to the Levantine spike that is the subject of the present work. Similarly, our method does not specify the spike geometry and therefore cannot rule out that features like those proposed by Davies and Constable (2017) exist in the simulation. However, the spike of Davies and Constable (2017) contained significant power in harmonic degrees above 100, while most of our simulations show good spatial convergence with truncations at degree 128 or below. Therefore, it is highly unlikely that such features are produced in the current simulations.

Finally, our approach implicitly assumes that the presence of spikes in a geodynamo simulation is not a necessary condition for that simulation to be considered Earth-like. We feel this is a reasonable viewpoint considering the present uncertainties in both spatial and temporal features of the Levantine spike; indeed, the purpose

of this study is to shed light on the enigmatic properties of geomagnetic spikes. A variety of criteria have been proposed for determining the similarity between geodynamo simulations and the geomagnetic field, including matching the morphology of the historical (Christensen et al., 2010; Amit et al., 2015) and Holocene (Davies and Constable, 2014) fields, the present pattern of secular variation (Mound et al., 2015) and features of the temporal power spectrum (Olson et al., 2012; Davies and Constable, 2014). We have followed the work of Davies and Constable (2014), which quantifies the level of spatio-temporal resemblance between simulations and observations and provides a rationale for selecting the simulations to study. The algorithm we have developed can be applied to different simulations in the future. It could also be used to determine morphological similarity between simulations and the paleofield once constraints on the spatio-temporal features of spikes are better understood.

If the rate of change given by Ben-Yosef et al. (2017) is appropriate for the Levantine spike then our results suggest that this event is compatible with an origin in the liquid core. Local changes with $\partial F/\partial t \sim 1\ \mu T yr^{-1}$ are at the upper end of values from our simulations. While we cannot rule out a dynamo origin for events with rates of $4-5\ \mu T yr^{-1}$, our simulations suggest that such events are very uncommon.

Strongly localised surface intensity anomalies with closed contours, a suggested morphology for the Levantine spike (Davies and Constable, 2017), are absent from the present simulations (see examples in Figures 5 and 6). Such features may arise in geodynamo simulations that are conducted at more extreme conditions, but we have no way to assess this. Alternatively, the Levantine spike may not be as confined in longitude as previously suggested. Davies and Constable (2017) have already noted that removing the data points with highest uncertainties in their compilation (Mali, Czech Republic, India, Greece, Syria and Egypt) would significantly improve the match between their synthetic spike and the data. This may also permit a

reasonable fit to the data with a wider synthetic spike, although this exercise must await a more robust scheme for assessing mutual compatibility among the available data for the Near East around 1000 BCE.

Our results suggest that extremal events are most likely to occur at latitudes above 50° and below 69° (the latitude of the tangent cylinder) due to migration of flux patches. Future paleomagnetic acquisitions that focus on these regions could be important for determining the regularity of spike events. Low-latitude features are certainly present in the simulations and can be approximately as intense as the high-latitude flux patches (see Figures 2 and 6 and also Davies et al. (2008)), similar to the modern field, so it does not appear that low-latitude variability is under-represented in the simulations. This interpretation suggests that the Levantine and Texan spikes are rare events. The simulations also suggest that there is no distinction between northern and southern hemispheres.

Extremal events in our simulations appear to reflect growth and migration of intense flux patches on the core-mantle boundary. In this interpretation, spike-shaped temporal features arise when an intensifying patch moves first towards and then away from the observation point. The patch must be sufficiently narrow or of the right geometry in order to generate the rapid intensity decline that follows the initial increase. In a sense this suggests that spikes are not unusual since dynamo simulations and global field models show that flux patches are a persistent feature of the geomagnetic field and are continually changing shape and amplitude (Amit et al., 2011). However, the amplitudes and rates of change associated with spikes suggest that these reflect patches that intensify and migrate faster than those seen in the historical field. Observing a spike may therefore be something of a chance event, dependent on having observations at just the right location and time to record the key phase of patch evolution.

5. Conclusions

The answers suggested by our study to the questions posed in the introduction are:

1. The most extreme intensity changes (extremal events) appear as spike-shaped events in the intensity time-series in some of our simulations; however, there are also examples where this is not the case. Instantaneous $(\partial F/\partial t)_{\max}$ can be larger than observed in the modern geomagnetic field regardless of the scaling used to redimensionalise simulation intensity, and match the lower end of estimates for the Levantine spike (Ben-Yosef et al., 2017; Korte and Constable, 2018). Extremal events are of larger scale than inferred for the Levant by Davies and Constable (2017); in particular they do not appear at the surface as regions of closed intensity contours. This could be because present dynamo simulations cannot capture such features, or because regional data with large age uncertainties used in the Davies and Constable (2017) compilation did not sample the spike. It is possible that our simulations contain spike-like temporal features that we have not detected, but these are not the fastest changes produced by the dynamo.
2. The most rapid intensity changes occur at high latitudes with $|\theta| > 50^\circ$ due to migration of flux patches. The Levantine region does not appear to sample faster changes than other regions.
3. $(\partial F/\partial t)_{\max}$ tends to arise just before an intense flux patch passes under the region. In these simulations the patches emerge from within the core and then intensify, so the location of $(\partial F/\partial t)_{\max}$ is not directly above an emerging flux patch. Extremal events tend to arise when the dipole moment is high and increasing, though whether this represents a causal relation awaits a more

detailed study of flux migration during these events.

We suggest that geomagnetic spikes do not reflect a novel physical process associated with the geodynamo. Rather, they reflect our inherently uneven sampling of the field: a spike is observed at locations that sample the growth phase of a particularly intense migrating flux patch. If correct, this interpretation suggests that geomagnetic spikes are not isolated events, though they may be seldom observed. Future data acquisitions at high latitudes represent a promising avenue for seeking further examples of rapid intensity changes.

Acknowledgements

CD acknowledges a Natural Environment Research Council personal fellowship, reference NE/H01571X/1. This work was also supported by NSF grant EAR1623786 for CC.

References

Amit, H., Deschamps, F., Choblet, G., 2015. Numerical dynamos with outer boundary heat flux inferred from probabilistic tomography–consequences for latitudinal distribution of magnetic flux. Geophys. J. Int. 203 (2), 840–855.

Amit, H., Korte, M., Aubert, J., Constable, C., Hulot, G., 2011. The time-dependence of intense archeomagnetic flux patches. J. Geophys. Res. 116, B12106.

Aubert, J., 2013. Flow throughout the Earth's core inverted from geomagnetic observations and numerical dynamo models. Geophys. J. Int. 192, 537–556.

544 Aubert, J., 2018. Geomagnetic acceleration and rapid hydromagnetic wave dynamics
545 in advanced numerical simulations of the geodynamo. Geophys. J. Int. 214 (1),
546 531–547.

547 Aubert, J., Gastine, T., Fournier, A., 2017. Spherical convective dynamos in the
548 rapidly rotating asymptotic regime. J. Fluid Mech. 813, 558–593.

549 Backus, G., 1983. Application of mantle filter theory to the magnetic jerk of 1969.
550 Geophys. J. R. Astr. Soc. 74 (3), 713–746.

551 Ben-Yosef, E., Millman, M., Shaar, R., Tauxe, L., Lipschits, O., 2017. Six centuries
552 of geomagnetic intensity variations recorded by royal Judean stamped jar handles.
553 Proc. Natl. Acad. Sci. 114 (9), 2160–2165.

554 Ben-Yosef, E., Tauxe, L., Levy, T. E., Shaar, R., Ron, H., Najjar, M., 2009. Geomag-
555 netic intensity spike recorded in high resolution slag deposit in Southern Jordan.
556 Earth Planet. Sci. Lett. 287 (3), 529–539.

557 Bourne, M. D., Feinberg, J. M., Stafford, T. W., Waters, M. R., Lundelius, E.,
558 Forman, S. L., 2016. High-intensity geomagnetic field 'spike' observed at ca. 3000
559 cal BP in Texas, USA. Earth Planet. Sci. Lett. 442, 80–92.

560 Brown, M. C., Donadini, F., Nilsson, A., Panovska, S., Frank, U., Korhonen, K.,
561 Schuberth, M., Korte, M., Constable, C. G., 2015. GEOMAGIA50. v3: 2. A new
562 paleomagnetic database for lake and marine sediments. Earth, Planets and Space
563 67 (1), 70.

564 Cai, S., Jin, G., Tauxe, L., Deng, C., Qin, H., Pan, Y., Zhu, R., 2017. Archaeointen-
565 sity results spanning the past 6 kiloyears from eastern China and implications for
566 extreme behaviors of the geomagnetic field. Proc. Natl. Acad. Sci. 114 (1), 39–44.

567 Christensen, U., 2010. Dynamo scaling laws and applications to planets. Space Sci.
568 Rev. 152, 565–590.

569 Christensen, U., Aubert, J., 2006. Scaling properties of convection-driven dynamos
570 in rotating spherical shells and application to planetary magnetic fields. Geophys.
571 J. Int. 166, 97–114.

572 Christensen, U., Aubert, J., Hulot, G., 2010. Conditions for Earth-like geodynamo
573 models. Earth Planet. Sci. Lett. 296, 487–496.

574 Constable, C., Korte, M., Panovska, S., 2016. Persistent high paleosecular variation
575 activity in southern hemisphere for at least 10 000 years. Earth Planet. Sci. Lett.
576 453, 78–86.

577 Davies, C., Constable, C., 2014. Insights from geodynamo simulations into long-term
578 geomagnetic field behaviour. Earth Planet. Sci. Lett. 404, 238–249.

579 Davies, C., Constable, C., 2017. Geomagnetic spikes on the core-mantle boundary.
580 Nat. Commun. 8, 15593.

581 Davies, C., Gubbins, D., 2011. A buoyancy profile for the Earth's core. Geophys. J.
582 Int. 187, 549–563.

583 Davies, C., Gubbins, D., Willis, A., Jimack, P., 2008. Time-averaged paleomagnetic
584 field and secular variation: Predictions from dynamo solutions based on lower
585 mantle seismic tomography. Phys. Earth Planet. Int. 169, 194–203.

586 Davies, C., Pozzo, M., Gubbins, D., Alfè, D., 2015. Constraints from material prop-
587 erties on the dynamics and evolution of Earth's core. Nat. Geosci. 8, 678–687.

588 Deguen, R., Alboussière, T., Labrosse, S., 2018. Double-diffusive translation of
589 Earths inner core. Geophys. J. Int. 214 (1), 88–107.

590 Driscoll, P., 2016. Simulating 2 Ga of geodynamo history. Geophys. Res. Lett. 43 (11),
591 5680–5687.

592 Driscoll, P., Olson, P., 2009. Polarity reversals in geodynamo models with core evo-
593 lution. Earth Planet. Sci. Lett. 282, 24–33.

594 Dziewonski, A., Anderson, D., 1981. Preliminary Reference Earth Model. Phys. Earth
595 Planet. Int. 25, 297–356.

596 Ertepinar, P., Langereis, C., Biggin, A., Frangipane, M., Matney, T., Ökse, T.,
597 Engin, A., 2012. Archaeomagnetic study of five mounds from Upper Mesopotamia
598 between 2500 and 700 BCE: Further evidence for an extremely strong geomagnetic
599 field ca. 3000 years ago. Earth Planet. Sci. Lett. 357, 84–98.

600 Finlay, C. C., Aubert, J., Gillet, N., 2016. Gyre-driven decay of the Earths magnetic
601 dipole. Nat. Commun. 7, 10422.

602 Fournier, A., Gallet, Y., Usoskin, I., Livermore, P. W., Kovaltsov, G. A., 2015. The
603 impact of geomagnetic spikes on the production rates of cosmogenic 14C and 10Be
604 in the Earth's atmosphere. Geophys. Res. Lett. 42 (8), 2759–2766.

605 Gallet, Y., Montaña, M. M., Genevey, A., García, X. C., Thébault, E., Bach, A. G.,
606 Le Goff, M., Robert, B., Nachasova, I., 2015. New Late Neolithic (c. 7000–5000
607 BC) archeointensity data from Syria. Reconstructing 9000 years of archeomagnetic
608 field intensity variations in the Middle East. Phys. Earth Planet. Int. 238, 89–103.

609 Garnero, E., McNamara, A., Shim, S.-H., 2016. Continent-sized anomalous zones
610 with low seismic velocity at the base of Earth's mantle. Nat. Geosci. 9, 481–489.

611 Gubbins, D., Willis, A., Sreenivasan, B., 2007. Correlation of Earth's magnetic field
612 with lower mantle thermal and seismic structure. Phys. Earth Planet. Int. 162,
613 256–260.

614 Heimpel, M., Evans, M., 2013. Testing the geomagnetic dipole and reversing dynamo
615 models over Earths cooling history. Phys. Earth Planet. Int. 224, 124–131.

616 Jackson, A., 2003. Intense equatorial flux spots on the surface of the Earth's core.
617 Nature 424, 760.

618 Jones, C., 2014. A dynamo model of Jupiter's magnetic field. Icarus 241, 148–159.

619 Kapper, K. L., Donadini, F., Hirt, A. M., 2015. Holocene archeointensities from mid
620 European ceramics, slags, burned sediments and cherts. Phys. Earth Planet. Int.
621 241, 21–36.

622 King, E., Buffett, B., 2013. Flow speeds and length scales in geodynamo models:
623 The role of viscosity. Earth Planet. Sci. Lett. 371–372, 156–162.

624 Korte, M., Constable, C., 2018. Archeomagnetic intensity spikes: Global or regional
625 geomagnetic field features? Front. Earth Sci. 6:17.

626 Kovacheva, M., Kostadinova-Avramova, M., Jordanova, N., Lanos, P., Boyadzhiev,
627 Y., 2014. Extended and revised archaeomagnetic database and secular variation
628 curves from Bulgaria for the last eight millennia. Phys. Earth Planet. Int. 236,
629 79–94.

630 Kutzner, C., Christensen, U., 2002. From stable dipolar towards reversing numerical
631 dynamos. Phys. Earth Planet. Int. 131, 29–45.

632 Lhuillier, F., Fournier, A., Hulot, G., Aubert, J., 2011. The geomagnetic secular-
633 variation timescale in observations and numerical dynamo models. Geophys. Res.
634 Lett. 38, L09306.

635 Livermore, P. W., Fournier, A., Gallet, Y., 2014. Core-flow constraints on extreme
636 archeomagnetic intensity changes. Earth Planet. Sci. Lett. 387, 145–156.

637 Masters, G., Laske, G., Bolton, H., Dziewonski, A., 2000. The relative behavior of
638 shear velocity, bulk sound speed, and compressional velocity in the mantle: impli-
639 cations for chemical and thermal structure. In: Karato, S., Forte, A., Liebermann,
640 R., Masters, G., Stixrude, L. (Eds.), Earth's deep interior: mineral physics and
641 tomography from the atomic to the global scale. Geophysical Monograph Series,
642 pp. 63–87.

643 Matsui, H., Heien, E., Aubert, J., Aurnou, J. M., Avery, M., Brown, B., Buffett,
644 B. A., Busse, F., Christensen, U. R., Davies, C. J., et al., 2016. Performance
645 benchmarks for a next generation numerical dynamo model. Geochem. Geophys.
646 Geosys. 17 (5), 1586–1607.

647 Mound, J., Davies, C., Silva, L., 2015. Inner core translation and the hemispheric
648 balance of the geomagnetic field. Earth Planet. Sci. Lett. 424, 148–157.

649 Nilsson, A., Holme, R., Korte, M., Suttie, N., Hill, M., 2014. Reconstructing Holocene
650 geomagnetic field variation: new methods, models and implications. Geophys. J.
651 Int. 198 (1), 229–248.

652 Olson, P., Christensen, U., 2002. The time-averaged magnetic field in numerical
653 dynamos with non-uniform boundary heat flow. Geophys. J. Int. 151, 809–823.

Olson, P., Christensen, U., Driscoll, P., 2012. From superchrons to secular variation: A broadband dynamo frequency spectrum for the geomagnetic dipole. Earth Planet. Sci. Lett. 319–320, 75–82.

Pavòn-Carrasco, F., Osete, M., Torta, J., De Santis, A., 2014. A geomagnetic field model for the Holocene based on archaeomagnetic and lava flow data. Earth Planet. Sci. Lett. 388, 98–109.

Pozzo, M., Davies, C., Gubbins, D., Alfè, D., 2014. Thermal and electrical conductivity of solid iron and iron-silicon mixtures at Earth's core conditions. Earth Planet. Sci. Lett. 393, 159–164.

Schaeffer, N., Jault, D., Nataf, H.-C., Fournier, A., 2017. Turbulent geodynamo simulations: a leap towards Earths core. Geophys. J. Int. 211 (1), 1–29.

Shaar, R., Ben-Yosef, E., Ron, H., Tauxe, L., Agnon, A., Kessel, R., Jan. 2011. Geomagnetic field intensity: How high can it get? How fast can it change? Constraints from Iron Age copper slag. Earth Planet. Sci. Lett. 301, 297–306.

Shaar, R., Tauxe, L., Ben-Yosef, E., Kassianidou, V., Lorentzen, B., Feinberg, J. M., Levy, T. E., 2015. Decadal-scale variations in geomagnetic field intensity from ancient Cypriot slag mounds. Geochem. Geophys. Geosys. 16 (1), 195–214.

Shaar, R., Tauxe, L., Gogichaishvili, A., Rathert, M. C., Devidze, M., Licheli, V., 2013. Absolute geomagnetic field intensity in Georgia during the past 6 millennia. Latinmag Lett. 3, 1–4.

Shaar, R., Tauxe, L., Ron, H., Ebert, Y., Zuckerman, S., Finkelstein, I., Agnon, A., 2016. Large geomagnetic field anomalies revealed in Bronze to Iron Age archeo-

676 magnetic data from Tel Megiddo and Tel Hazor, Israel. Earth Planet. Sci. Lett.
677 442, 173–185.

678 Stelzer, Z., Jackson, A., 2013. Extracting scaling laws from numerical dynamo mod-
679 els. Geophys. J. Int. 193 (3), 1265–1276.

680 Thébault, E., Finlay, C. C., Beggan, C. D., Alken, P., Aubert, J., Barrois, O.,
681 Bertrand, F., Bondar, T., Boness, A., Brocco, L., et al., 2015. International ge-
682 omagnetic reference field: the 12th generation. Earth, Planets and Space 67 (1),
683 79.

684 Willis, A., Sreenivasan, B., Gubbins, D., 2007. Thermal core-mantle interaction:
685 exploring regimes for 'locked' dynamo action. Phys. Earth Planet. Int. 165, 83–92.

686 Wong, J., Davies, C., Jones, C., 2018. A Boussinesq slurry model of the F-layer at
687 the base of Earth's outer core. Geophys. J. Int. 214, 2236–2249.

E	Pm	Ra	$q^\star$	BC	Length	Revs	Rm	$\theta_{\max}$	$(\partial F/\partial t)_{\max}$
5×10^{-4}	5	250	0	FFFF	10.6 (431)	Y	225	54	1.36
5×10^{-4}	5	350	0	FFFF	13.3 (607)	Y	252	62	0.78
1.2×10^{-4}	10	150	0.9	FTFF	0.37 (24)	N	351	-56	0.31
1.2×10^{-4}	10	34.9	0.3	FTFF	10.8 (195)	N	108	-48	0.55
1.2×10^{-4}	10	34.9	0.9	FTFF	9.3 (228)	N	135	-64	0.39
5×10^{-4}	10	250	0	FFFF	3.33 (193)	N	386	36	0.44
1.2×10^{-4}	10	300	0	FTFF	1.87 (177)	N	540	66	0.38
5×10^{-4}	10	350	0	FFFF	5.1 (415)	Y	450	68	0.76
1.2×10^{-4}	10	450	0	FTFF	0.31 (31)	N	684	50	0.39

Table 1: Runs used in this study. The Ekman number E, magnetic Prandtl number Pm, Rayleigh number Ra and amplitude of boundary heat flow heterogeneity $q^\star$ (=0 for homogeneous boundaries) are input parameters to the simulation along with the Prandtl number which is always set to unity. BC refers to the thermal boundary conditions used: FF is fixed flux; FT is fixed temperature; first column refers to the inner boundary; second column refers to the outer boundary. Length gives the number of magnetic diffusion times in each run and the corresponding run length in kyrs (brackets) using the advective time scaling. Revs denotes whether the simulation exhibits polarity reversals (Y) or not (N). The magnetic Reynolds number Rm is a simulation output. The last two columns provide the latitude (in degrees) and amplitude (in μT yr^{-1}) of the maximum intensity change to aid comparison with the Figures.

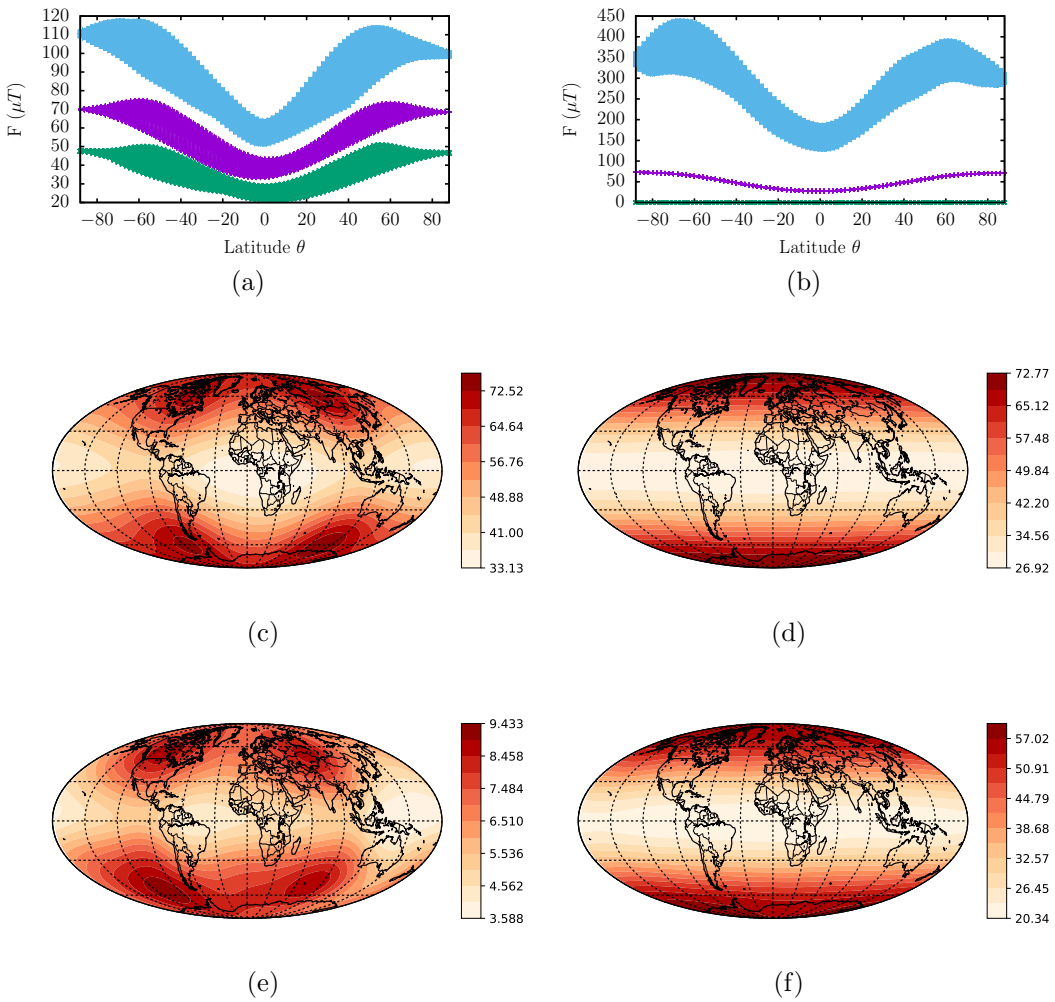

Figure 1: Intensity diagnostics for dynamo solutions with $Rm = 135$ (left column) and $Rm = 252$ that use different input parameters (see Table 1). Top row: maximum (blue), minimum (green) and average (purple) F at each longitude as a function of latitude (note that south polar average is normalised to 70 μT). Middle: average F in Mollweide projection. Bottom: standard deviation of F in Mollweide projection. All plots show F at Earth's surface.

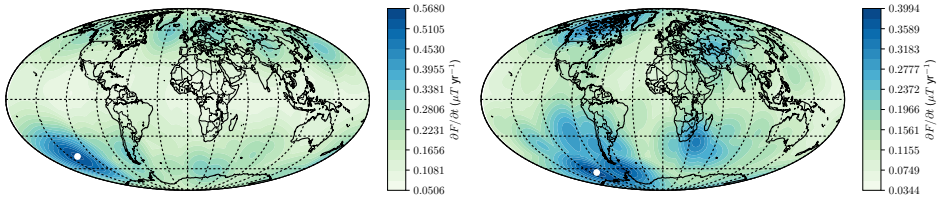

(a)$Rm = 108, q^\star = 0.3$ (b) $Rm = 135, q^\star = 0.9$

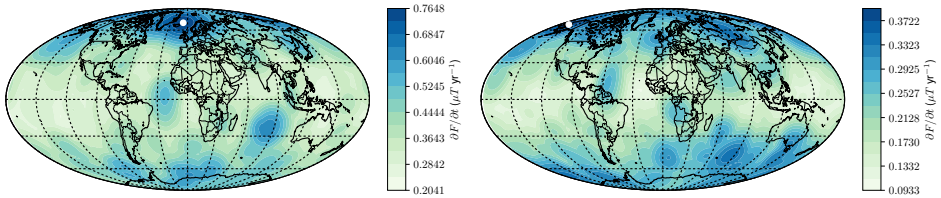

(c) $Rm = 450$ (d) $Rm = 540$

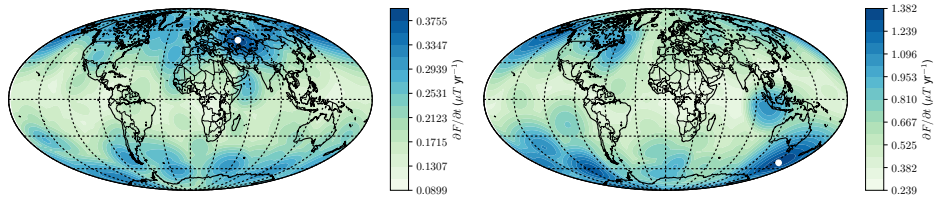

(e) $Rm = 684$ (f) $Rm = 225$

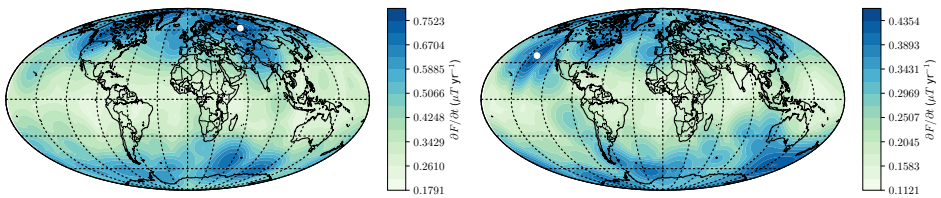

(g) $Rm = 252$ (h) $Rm = 386$

Figure 2: Mollweide projection at Earth's surface of maximum $\partial F/\partial t$ ($\mu T yr^{-1}$) for eight of the simulations described in Table 1. Note that values at each location may not have occurred at the same point in time. White dots show the location of largest $\partial F/\partial t$ on each plot.

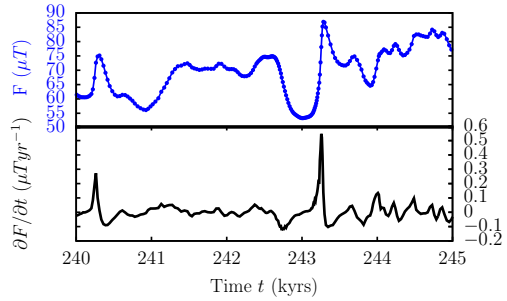

(a) $Rm = 108$

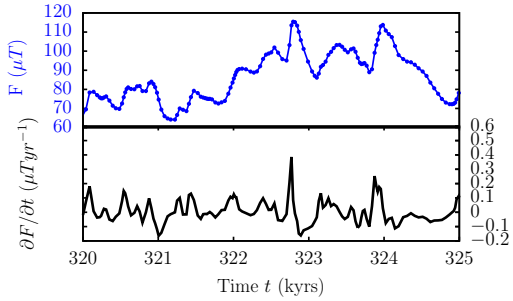

(b) $Rm = 135$

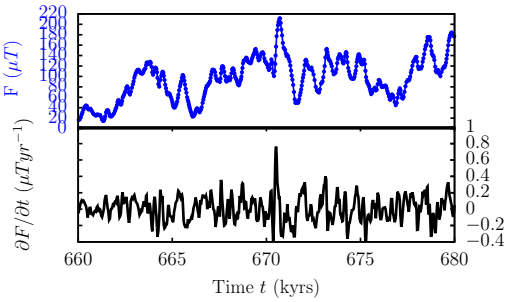

(c) $Rm = 450$

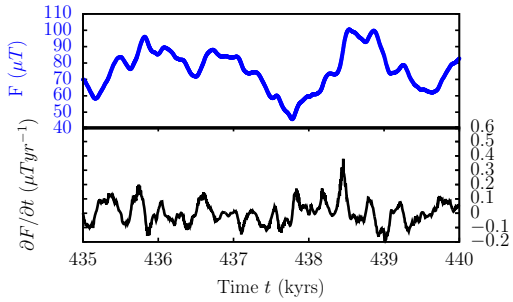

(d) $Rm = 540$

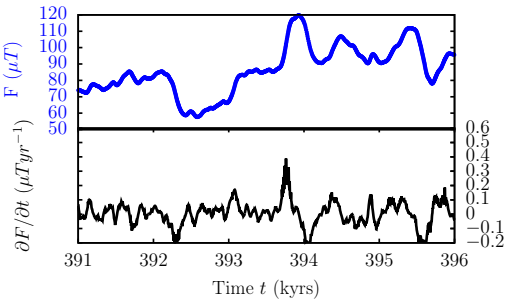

(e) $Rm = 684$

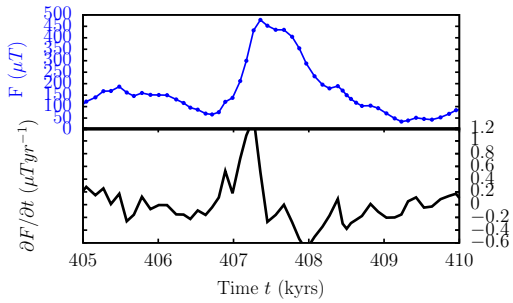

(f) $Rm = 225$

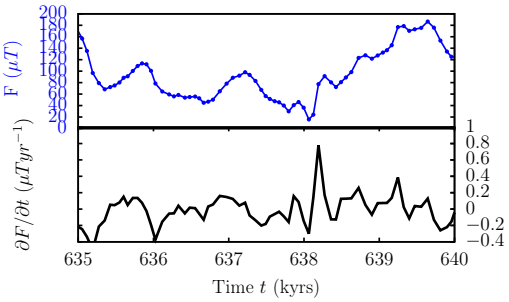

(g) $Rm = 252$

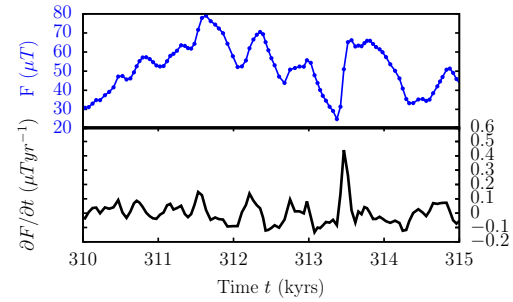

(h) $Rm = 386$

Figure 3: Time-series of $\partial F/\partial t$ at Earth's surface for various simulations. Time-series are taken at the location shown by the white dots in Figure 2 encompassing the moment of maximum intensity change.

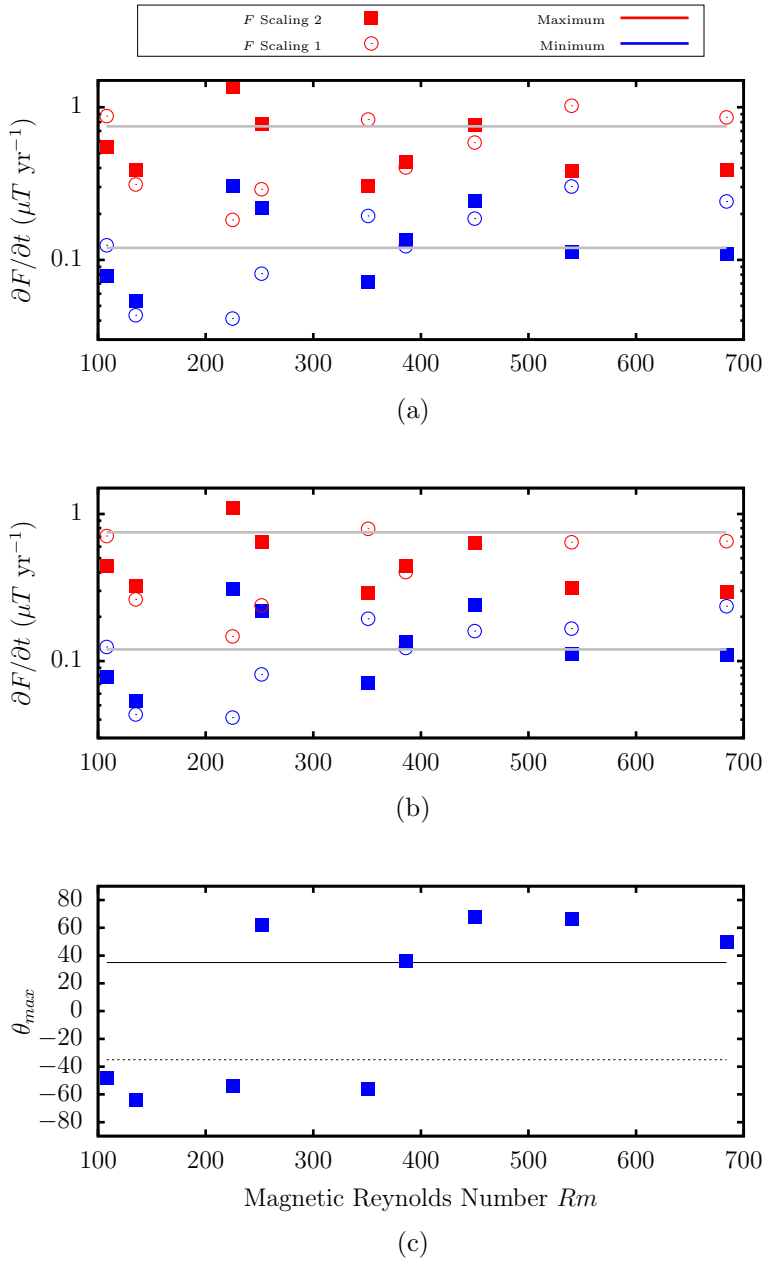

Figure 4: Summary of results for all simulations in Table 1. Red (blue) points show the highest (lowest) maximum in $(\partial F/\partial t)_{\max}$ having scanned over all locations with latitude cutoff of $\theta_c = 90°$ (top) and $\theta_c = 35°$ (middle). Solid squares show results for intensity scaling (2) while open circles show intensity scaling (1). Horizontal lines show the value of 0.18 $\mu T yr^{-1}$ for the modern field and the lower estimates for the Levantine spike (Ben-Yosef et al., 2017). Bottom panel shows the latitude at which the maximum change in $\partial F/\partial t$ is obtained on Earth's' surface for the 90° cutoff.

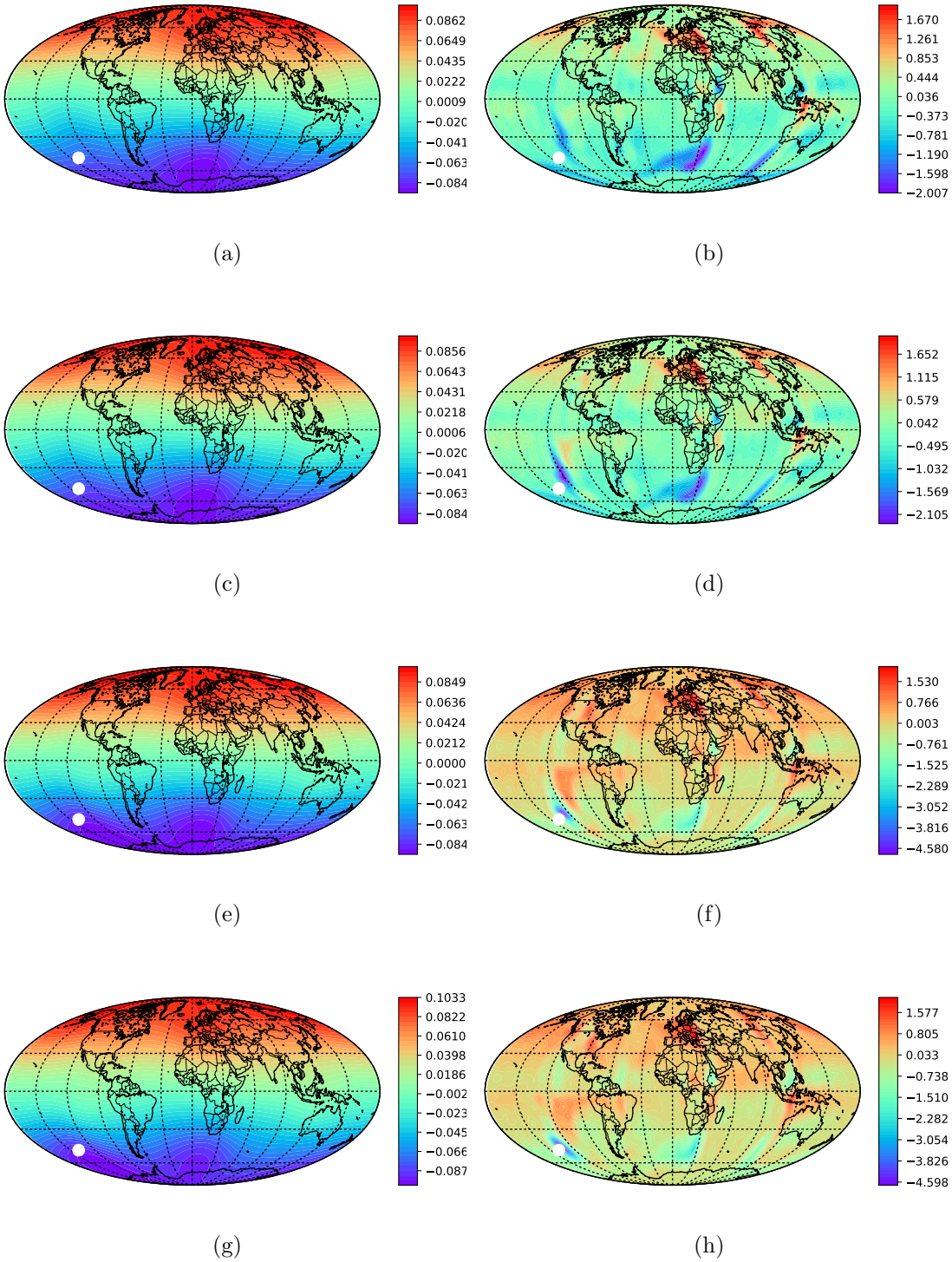

Figure 5: Dimensionless radial magnetic field at the surface (left) and CMB (right) for the simulation with $Rm = 108$ at four times (increasing from top to bottom) spanning the largest intensity change in the simulation (Figures 2 and 3). The site of largest change is shown by the white marker. The maximum change is between rows 2 and 3. Note that the colour scale is arbitrary since the actual intensity values are not important here.

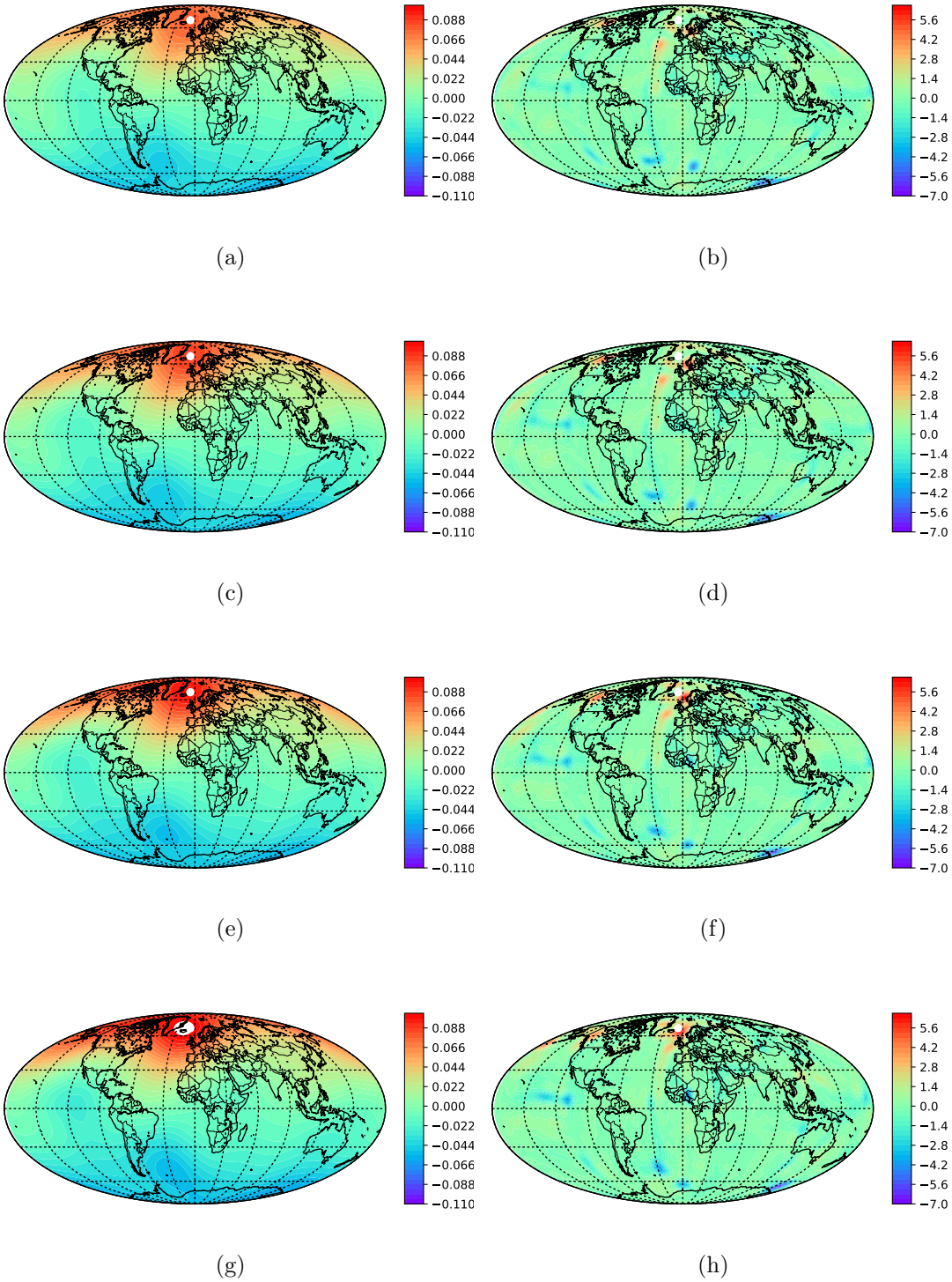

Figure 6: Dimensionless radial magnetic field at the surface (left) and CMB (right) for the simulation with $Rm = 450$ at four times (increasing from top to bottom) spanning the largest intensity change in the simulation (Figures 2 and 3). The site of large change is shown by the white marker. Note that the colour scale is arbitrary since the actual intensity values are not important here.

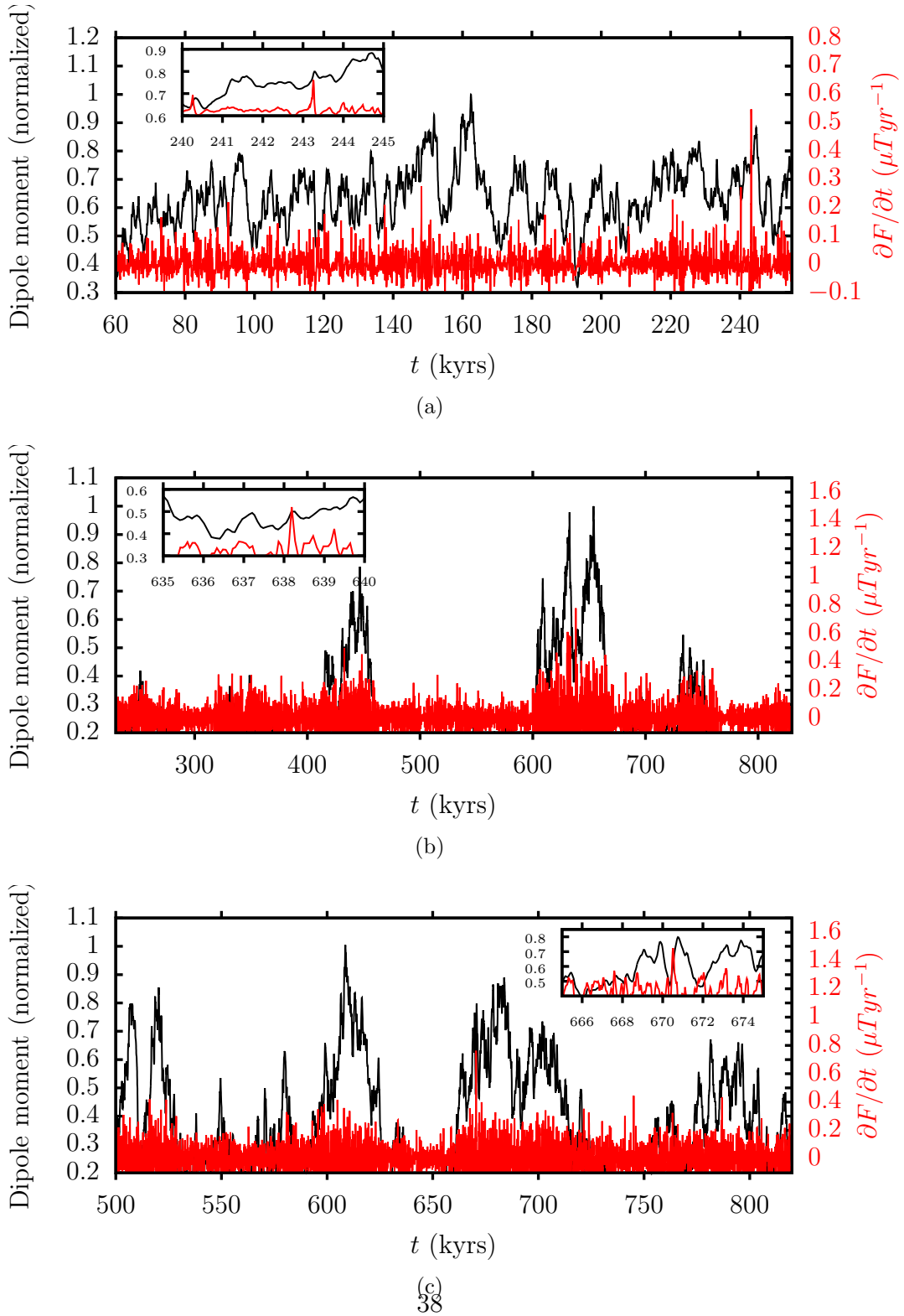

Figure 7: Dimensionless dipole moment (black) and $\partial F/\partial t$ (red) at the site with maximum $(\partial F/\partial t)_{\max}$ (shown in white markers in Figure 2) for runs with $Rm = 108$ (top), $Rm = 252$ (middle) and $Rm = 450$ (bottom). Insets zoom in on the time surrounding the maximum intensity change corresponding to the extremal event.